Synthesis and characterization of Mn:CdS nanoflower thin films prepared by hydrothermal method for photocatalytic activity

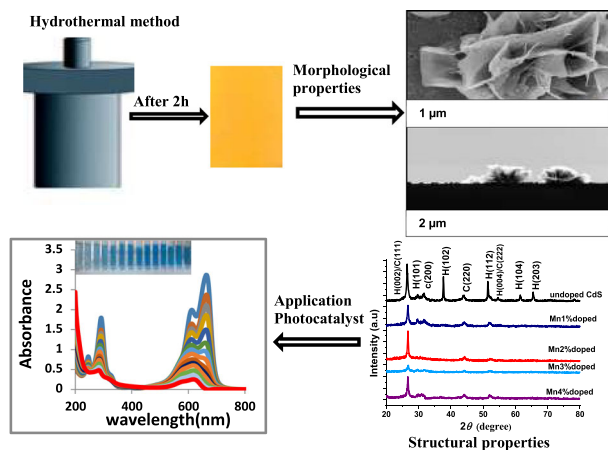Selma M. H. AL-Jawad[1] · Natheer Jamal Imran[2] · Kahlaa H. Aboud[1]

Abstract

Mn-CdS nanoflowers were successfully deposited using hydrothermal technique at 150 °C for 2 h. The effect of changing the dopant concentration on the structural, morphological and optical properties of the produced samples was investigated. The XRD diffraction technique showed the formation of hexagonal and cubic phases, whereas the FE-SEM analysis confirmed the success of the formation of flower-like nanostructures. The UV–Visible spectra revealed that the energy band-gap values decreased with increasing manganese concentrations. The optical band-gap ranges were 2.4, 2.35, 2.25, 2.14 and 1.76 eV thin films with concentrations of (0%, 1%, 2%, 3% and 4%) for undoped and Mn-doped cadmium sulfide. The results of UV–Vis spectroscopy agree with the conclusions of the PL study. The surface morphology was studied using scanning electron microscopy and atomic force microscopy. According to the results, the crystalline size decreased as doping concentrations increased. The Mn-doped cadmium sulfide films exhibited unprecedented photocatalytic activity for the decomposition of methyl blue (MB) and methyl violet (MV) dyes, due to high surface area, low energy gap and efficient charge separation properties for the prepared films.

Graphical Abstract

Synthesis and Characterization of Mn:CdS Nanoflower Thin Films Prepared by Hydrothermal Method for Photocatalytic Activity.

Preparation and Characterization of CdS prepared by hydrothermal method

✉ Selma M. H. AL-Jawad
   100069@uotechnology.edu.iq

1 Applied physics department, School of Applied Sciences,

   University of Technology, Baghdad, Iraq

2 Environment and Water Directorate, Ministry of Science and Technology, Baghdad, Iraq

1 Introduction

The recent emergence of nanostructure materials has attracted the attention of researchers in a variety of environmental niche areas due to their intriguing properties, size and surface effects, high specific surface area, lower density, increased permeability, unique optical properties and diverse possible applications. The physical and chemical characteristics of materials may be changed by altering their morphology [1]. Chalcogenides have gained considerable interest due to their usefulness in a wide range of optoelectronic devices [2]. Cadmium sulfide (CdS) is a major II-VI semiconductor with a direct optical band gap (2.4 eV at ambient temperature), high refractive index (2.5), high absorption coefficient (10^4–10^5 cm^{-1}), high mobility (0.1–10 cm^2 V^{-1} S^{-1}), small exaction Bohr radius and compact dimensions (2.5 nm) [3]. CdS has two crystalline forms: a hexagonal phase (wurtzite) and a cubic phase (zinc mixing). CdS films in both of these phases can be developed [4]. CdS thin film can be deposited by various methods, such as chemical bath deposition [5], sol-gel synthesis [6], thermal evaporation [7], electrodeposition [8], sputtering [9], spray pyrolysis [10], hydrothermal [11] and microwave heating [12]. Each technique has produced films with a wide range of characteristics that can be tailored to specific applications. However, CdS thin films have been developed using a variety of techniques. Some of these methods are complex, but hydrothermal processing has many advantages. These include high component purity, homogeneity, crystal symmetry, scale distributions, narrow particles, cost-effectiveness, high yield and the potential to achieve a controlled morphology [12]. There are numerous potential uses for nanostructured CdS. Since cadmium sulfide has a visible region bandgap, it can effectively use solar energy for photocatalytic. CdS are widely used in solar optoelectronics, lasers, photoconductors, light-emitting diodes, transistors, and biological applications. Semiconductor photocatalytic activity very closely associates with its microstructures, which, under special growth conditions, is substantially dominated by crystal growth mechanisms. The morphology, size, and composition of crystals are key factors that affect light absorption and the efficacy of the photocatalytic system [13]. Various studies have developed CdS photocatalysts for photoactivation with various morphologies [4]. Various methods, such as metal-ion doping, metal injection, and compositing with other components, were used to achieve a realistic approach to increase photocatalytic activity. Metal-ion doping, for example, can increase photocatalytic performance by changing the bandgap [14]. The adding impurities to CdS are critical to its effectiveness in advanced applications. Recently, the addition of trace quantities of dopants to CdS hosts has gained a lot of interest to improve structural, optical, and electrical transport features [15].

The addition of metallic ions such as Fe^{2+}, Co^{2+}, Mn^{2+}, Mg^{2+}, and Ni^{2+}, to the CdS thin film, has vigorously impacted the optical and magnetic properties [16]. Where, Mn^{2+} has a smaller standard ion radius (0.046 nm) than Cd^{2+} (0.097 nm), despite this, its Pauling electronegativity (1.55) is comparable to Cd^{2+} (1.61), as a result of this, CdS can be doped with Mn^{2+} [17]. The manufacture of CdS films doped with magnetic ions such as Mn has lately attracted renewed attention [18]. Delikanli et al. [19] studied the magnetic characteristics of Mn-doped CdS Nanorods, a significant ferromagnetic hysteresis loop was also discovered. Bhattacharyya et al. [20] doped CdS with different atomic percents of Mn (0, 0.9, 1.2, 1.8, and 2.4), and studied the structural and magnetic properties for it. In this study, we have investigated structural, optical, and morphological changes to examine how Mn doping impacts CdS thin films. CdS with variable Mn doping concentrations was deposited on a glass substrate using a hydrothermal method. The photocatalytic properties of Mn: doped CdS were then studied. We addressed a suggested photocatalytic mechanism that might explain the catalytic activity of Mn-improved CdS. There are some research reports on doping CdS with transition metals [17–20] the physical properties have been studied by most of the researchers and the studies on physical and photocatalytic properties of Mn: CdS prepared by the hydrothermal method are very limited and need more understanding. Therefore, in this work, the structural, morphological, optical, and photocatalytic properties of pure and Mn-doped CdS thin films have been studied. A photocatalytic activity has been determined to Mn:CdS nanostructure by testing methyl blue and methyl violet (MV) dyes under xenon radiation.

2 The experimental

2.1 Hydrothermal process preparation of CdS and Mn-CdS thin films

Cadmium sulfide (CdS) films were deposited using hydrothermal technique on glass substrates, after which the glass substrates were submerged for 8 h in hydrochloric acid and then subjected to ultrasound cleaning with acetone and deionized water. First, 20 ml of 0.05 M ($3CdSO_4.8H_2O$) was added, Manganese (II) sulfate ($MnSO_4$) was blended slowly with add NH_3 Ammonia constant agitation in order to change the pH value of the resolution to 12, by using a magnetic stirrer. Then, with a continuous stirring for 15 min, 20 ml of 0.1 M thiourea was applied. Finally, the resulting solution was poured in a Teflon container, which includes a glass substrate that was sealed inside the autoclave (stainless steel) for hydrothermal processing. The autoclave was sealed and held for 2 h at 150 °C. After that, the autoclave was cooled at room

temperature. At the end of the preparation time, the autoclave was cooled to room temperature naturally. After that, the glass substrate was taken out and deionized water was used to clean it in an ultrasonic bath. The previous technique was repeated with various concentrations such as 1, 2, 3, and 4%.

2.2 Characterizations

The crystal composition of the generated CdS and Mn-doped CdS was determined by X-ray diffraction analysis (XRD-6000, Shimadzu, Japan) with Cu K radiation (=1.54056) for two in the 20°–80° range. A Shimadzu UV-1800 spectrophotometer was used to perform UV–Visible spectroscopy in the wavelength range of 200–1100 nm. Photoluminescence was performed by FLUORESCENCE (Varian) Hitachi Type S-4160 SN: EL05043810. The surface topography was assessed with AFM images (CSPM-5000). The Field-Emission Scanning Electron Microscope (FE-SEM) was used to examine the surface, using Zeiss Sigma 300- HV.

2.3 Photocatalytic experiment of Mn: CdS thin films

In this study, doped and undoped CdS thin films were used as photocatalysts to study the degradation of methyl blue (MB) and methyl valuate (MV) dye under a 40 mW xenon light. The photocatalytic experiments were carried out under the same conditions. To perform photocatalytic experiments, 0.01 mg of methyl blue or methyl valuate dye was dissolved in 1000 mL deionized water and stirred for 5 min. There was about a 15-centimeter distance, between the source and the aqueous solution. The samples were exposed to illumination with Xe lamp (Xenon lamp spectrum has the continuous spectrum through the visible and UV regions much like the solar spectrum) in the dye solution for up to 260 min for each sample. The reaction was maintained at room temperature. For 20-min intervals, the absorbance of (MB) and (MV) solutions was monitored. Photocatalytic degradation of methyl blue (MB) and methyl violet (MV) was monitored, using a UV–Vis spectrophotometer with a twin beam in a wavelength range of 300–1000 nm (UV-1800 Shimadzu). The degradation process performance was measured as a function of time using absorption at maximum absorption = 660 nm for MB and 585 nm for MV. The photocatalytic elimination, a pseudo-first-order reaction, was quantified using the formula [21].

$$1n \frac{C}{C_o} = -Kt \tag{1}$$

where C_0 represents the initial concentration of MB and MV (mg/l), C represents the concentration at each time interval in mg/l, (K) represents the rate constant, and t represents the irradiation time in minutes.

Removal (%) of methyl blue (MB) and methyl violet (MV) can be determined via the relation [21]:

$$Degradation(\%) = \left(\frac{C_o - C}{C_o} \right) \times 100 \tag{2}$$

3 Results and discussion

3.1 Structural properties

Figure 1 shows the XRD patterns of pure sample thin film, pure sample powder removed from the substrate and doped CdS thin films with different concentrations (1%, 2%, 3% and 4%) deposited on the base of the glass. The XRD pattern shows the mixed cubic and hexagonal phases of the deposited films. The detected peaks were at 26.4°, 29.7°, 31.6°, 37.6°,43.9°, 51.4°, 54.5°, 61.4° and 65.5°, corresponding to the lattice planes H (002)/C (111(, H (102), C (220), H (112), H (004)/C (222), H (104) and (203) of pure sample thin film and powder. The peak intensity of powder was higher than that from pure sample thin film. These results well agree with the standard (JCPDS No. 42-1411). In comparison to the other peaks, in pure and doped CdS film patterns, the highest intensity at (002) planes occurred, as illustrated in Fig. 1. It may be concluded that the preferred orientation is the polycrystalline character of the films that were preserved following Mn-ion implantation, according to XRD measurements. Furthermore, the peak intensity reduced along with increasing Mn-ion fluence, despite the fact that the (002) peak location scarcely changes. This might arise as a result of metal-ion doping and/or implantation-related damage.

The crystalline size of CdS (Gs) was computed according to the formula of the Shearer-Debye equation below [22].

$$Gs = \frac{A\lambda}{\Delta\theta \cos\theta} \tag{3}$$

where λ is the wavelength of x-ray radiation incident (1.54056 Å), k is the shape factor in form (0.94) and θ is the position of the peak. The results show that the crystalline size decreases with the increase of Mn impurity. The addition of manganese impurity was also observed, this was leading to an increase in FWHM, which is the explanation for the decrease in crystalline size. The size of the Mn: CdS nanocrystalline decreased from 10.7 to 7.43 nm along with increasing the doping concentration, as shown in Table 1. The hexagonal phase structure's lattice constants a and c were estimated based on the position of the XRD peaks by the equation below [23].

$$\frac{1}{d^2} = \frac{4}{3} \left[\frac{h^2 + hk + k^2}{a^2} \right] + \frac{l^2}{c^2} \tag{4}$$

where, it was found that the lattice parameters got changed after doping. The substitution of Mn ions for Cd ions due to Mn has a smaller atomic size than Cd, might be the cause for this lattice parameter shift [24]. Table 1 shows the modification of the Mn constants for the CdS nanostructure at different doping concentrations, where h, k, and l are Miller indicators.

The Williamson–Hall plot shows lattice strain as well as effective crystallite size. The strain in the lattice is computed by the slope of the best linear fit of the plate between βcosθ and 4sinθ, whereas the crystallite size is defined by the y-intercept, as illustrated in Fig. 2, by using the following equations [25]:

$$\beta_{hkl} = \beta_{Gs} + \beta_{\varepsilon} \tag{5}$$

$$\beta_{hkl} = 4\varepsilon \tan\theta + \left(\frac{k\lambda}{G_s \cos\theta}\right) \tag{6}$$

Rearrangement of the above equation yields [26]:

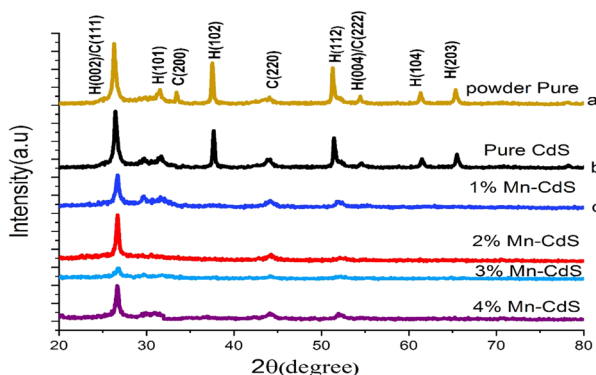$$\beta\cos\theta = 4\varepsilon\sin\theta + \frac{k\lambda}{Gs} \tag{7}$$

Fig. 1 XRD patterns of CdS and Mn-CdS doped

A negative slope in the plot indicates the presence of compressive strain for all samples, except for the Mn1% film that showed the positive slope, this indicates the presence possibility of tensile strain. The negative slope in the graphs indicates that the CdS films got subjected to compressive microstrain. The compressive strain is defined as the shrinking of a material structure based on the determination of lattice constants. The dislocation density is defined as the length of dislocation lines per unit volume of the crystal, Williamson and Smallman were used to measuring it [27].

$$\delta = \frac{1}{G_s^2} \tag{8}$$

Table 2 shows that increasing Mn concentration which causes an increase in dislocation densities. The greatest value of microstrain can be found at (3% Mn) because of the film's limited Nano size, this is conceivable.

3.2 Morphological properties of CdS

3.2.1 Atomic force microscopy (AFM)

One of the most important variables influencing optical and electrical qualities is morphology. Figure 3 illustrates 3D and cumulative distribution AFM images of pure and doped CdS thin films deposited by the hydrothermal process with Mn concentrations of 1%, 2%, 3% and 4% of the film. Figure 3a–c micrographs demonstrate that the thin CdS films have an extremely compact surface. The film is comprised of spherical-shaped particles that were stacked together and distributed uniformly in size. For this assay, the average grain size was 87.76, 65.06, 69.99, 67.7 and 83.27 nm for pure, 1%, 2%, 3% and 4% doping, respectively. The root means square is 5.3, 5.77, 8.59, 11.5, and 13.5 nm for pure, 1, 2,
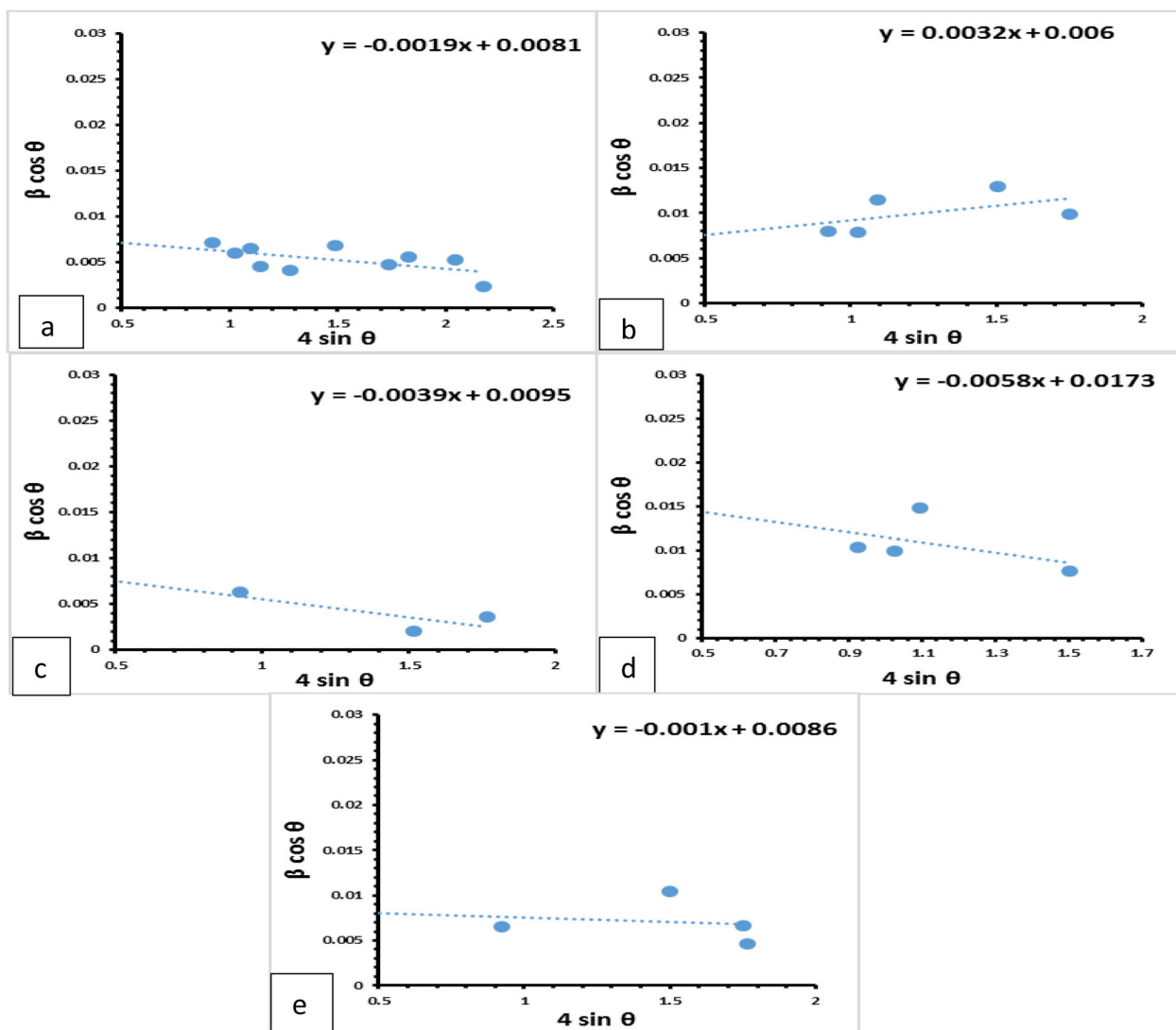
Table 1 Crystallite size, position of diffraction peaks (2θ), FWHM, and lattice constants of CdS thin films synthesized at 150 °C for undoped and Mn-CdS doped

CdS samples	Crystal structure	D (nm)	2θ(deg.) measured	(FWHM) Radiance	Lattice constants (Å)		
					a = b	c	c/a
Pure	Hexagonal CdS	10.746	26.547	0.4228	4.17878	6.716	1.607
Mn-CdS1%	Hexagonal CdS	9.591	26.709	0.473	4.142	6.669	1.61
Mn-CdS2%	Hexagonal CdS	12.192	26.721	0.372	4.193	6.666	1.6
Mn-CdS3%	Hexagonal CdS	7.438	26.792	0.61	4.1338	6.649	1.608
Mn-CdS4%	Hexagonal	11.671	26.703	0.388	4	6.67	1.667
Standard	JCPDS card no. 41-1049				4.14092	6.7198	1.6228

Fig. 2 Williamson–Hall (W–H) plot of doped CdS thin films with various Mn. **a** For pure sample. **b** 1% Mn. **c** 2% Mn. **d** 3% Mn. **e** 4% Mn sample.

Table 2 Crystallite size, lattice microstrain values, and dislocation density of CdS thin films undoped and Mn-doped

Sample	Gs (nm) Scherrer method	Gs (nm) W–H method	Dislocation density ($\delta \times 10^{-3}$) (Lines/nm^2)	Microstrain (ε)
Pure CdS	10.746	18.55	8.65	−0.0022
Mn-CdS (1%)	9.591	24.78	10.87	0.0032
Mn-CdS (2%)	12.192	15.61	6.72	−0.0039
Mn-CdS (3%)	7.438	8.54	18.07	−0.0058
Mn-CdS (4%)	11.671	17.309	7.34	−0.0009

3, and 4% doping, respectively. And the roughness average is about 4.58, 1.8, 7.44, 9.86, and 11.7 nm for pure, 1, 2, 3, and 4% doping, respectively. The film for 3% and 4% is made up of round-shaped cylindriform (tubes) grouped together in regular size distribution, as seen in Fig. 3c, d, between these holes, there is also some empty space.

3.2.2 Field-emission scanning electron microscopy

Figs. 4 and 5, show images of undoped and 1% Mn-doped cadmium sulfide. Obviously, the first two samples have nano-like flakes. The vertically-aligned nano flakes uniformly grew on a large scale on the substrate, with the majority of them intersecting to form a network structure.
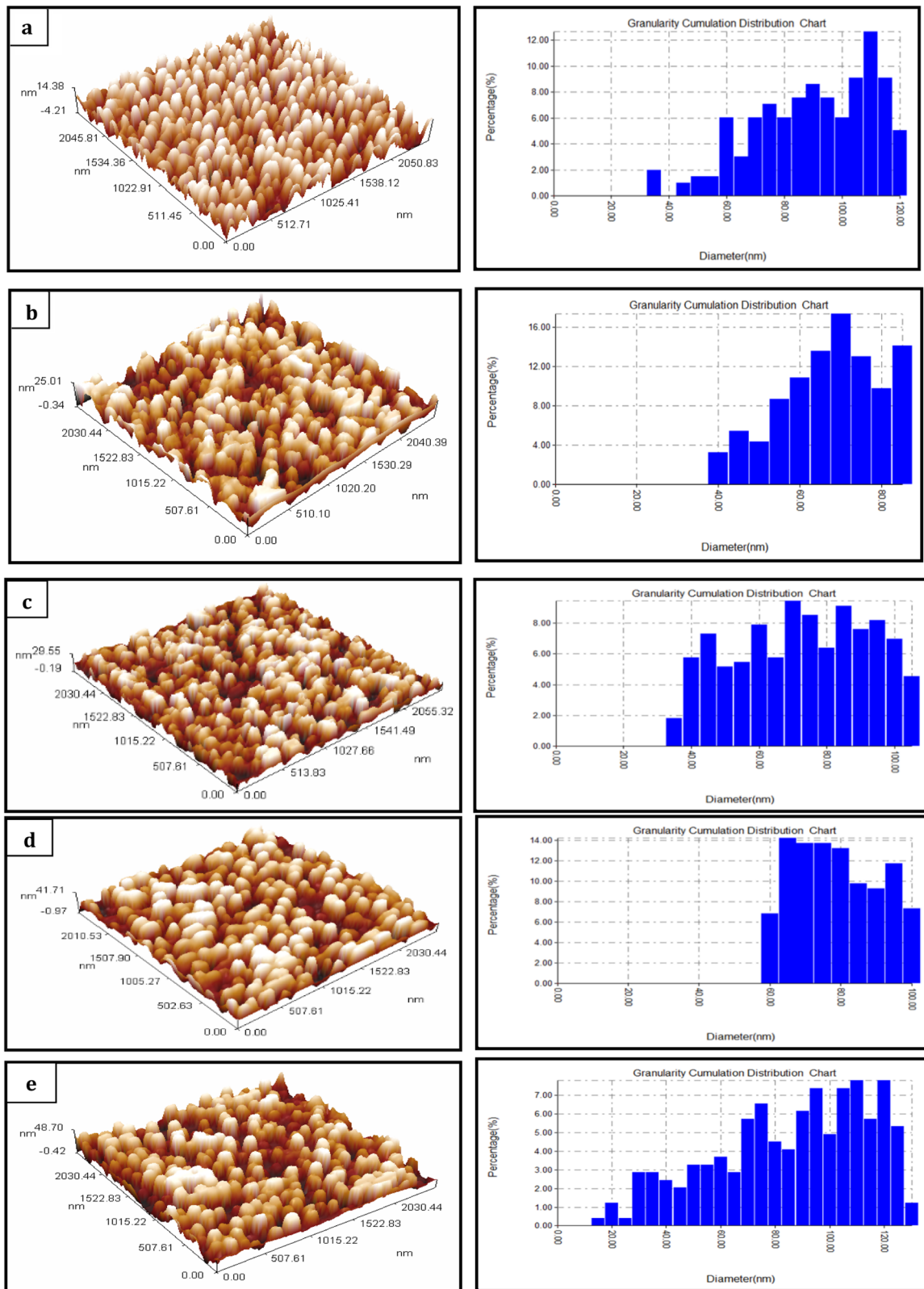
Fig. 3 Granularity cumulative distribution report and AFM image of CdS thin film pure and Mn-doped CdS films in 3D (a) pure, (b) Mn1%, (c) Mn2%, (d) Mn3%, (e) Mn4%
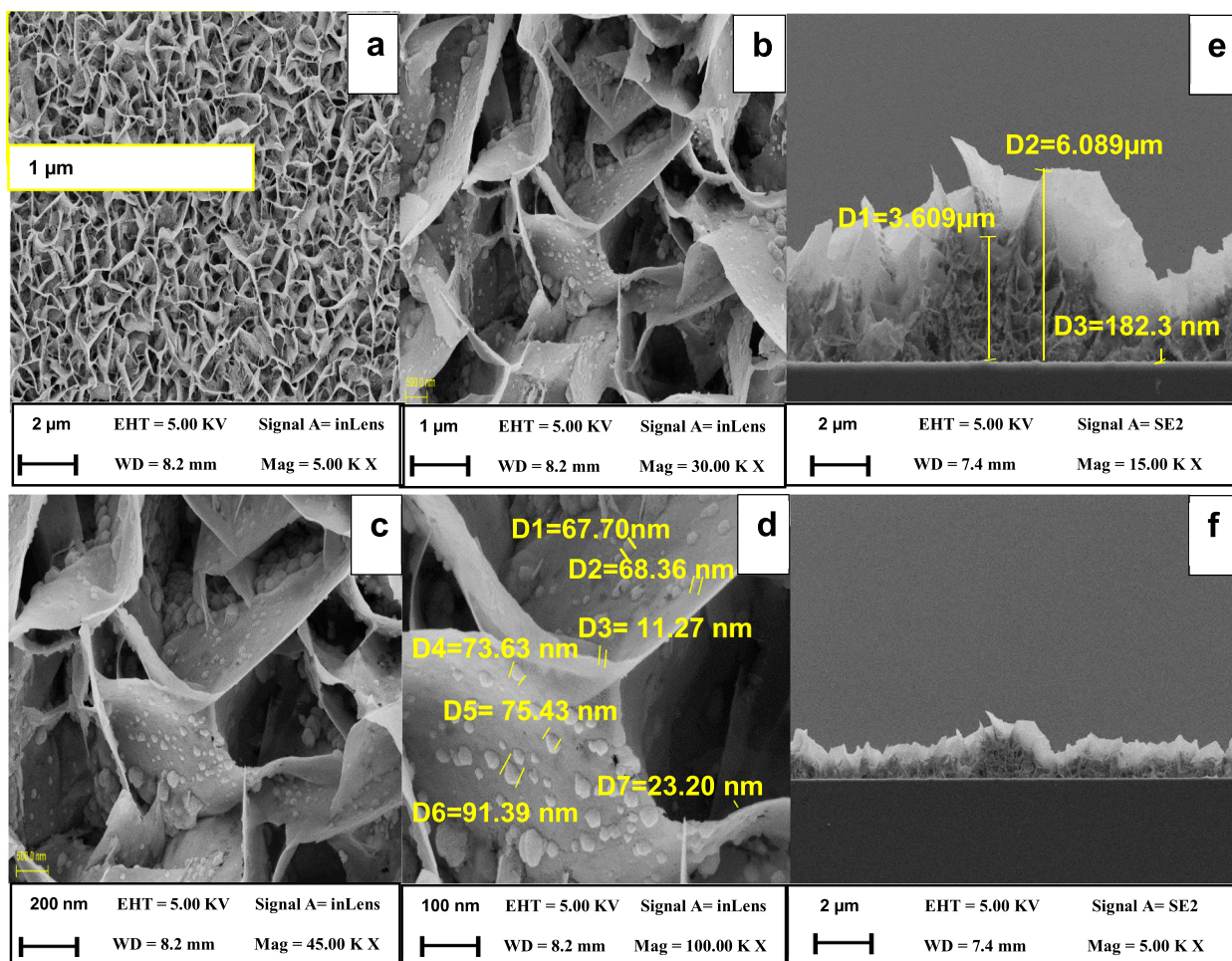
Fig. 4 Pure CdS FESEM images (**a**, **b**) low magnification (**c**, **d**) high magnification top view (**e**, **f**) cross-sectional view

The two samples demonstrate a wide specific region composed of nanoplates, because of the porous structure. PEC investigations and photocatalytic activity benefit greatly from such morphology [28]. The images in Fig. 4 and with high magnification appear the surface of nano plates cover with a lots of tiny nano plates. A field-emission scanning electron microscope (FE-SEM) was used to investigate the thickness, structure, and morphology of pure and doped CdS thin films which was made by using the hydrothermal technique. The cross-sectional images of FE-SEM in Figs. 4 and 5 illustrate the film that has been placed in an uneven pattern. The CdS films, on the other hand, showed good adherence. Furthermore, it was found that the CdS pure and doped 1% Mn films have a thickness of 6.089 and 7.219 μm, respectively.

CdS doped with 2%, was obviously made up of a plethora of hierarchical flower-like nanostructure aggregates. The blooms are similar in form but vary in size. As illustrated in Fig. 6, a single flower has a spheroidal hierarchical nanostructure with an average length of 6.599 μm. Furthermore, each flower is composed of a vast number of

Nano sheets that interact with one another to form hierarchical flower-like structures. Each flower's surface is porous, and each Nano sheet has an uneven border. There are several barriers and porous surfaces, they are extremely rough with thickness equal 8.203–175.0 nm for 2% Mn-CdS doped sample. The cross-section shows a layer of flower-like structures which is uniformly covered on the CdS thin film substrate. The CdS flowers have an average cross-section diameter and length of 601.6 nm and 6.599 μm, respectively.

The nanosheets have become bigger and longer (for CdS doped with 3%), as illustrated in Fig. 7, this results in a full flower-like structure. All of the nanosheets are connected to one another via a fundamental quasisphere core, giving the flower its spherical form. With high magnification, the flower-like CdS is grouped and mixed to produce network-shaped nanosheets films, assembling into flower-like structures as a whole, they are extremely rough with a thickness which equals 45.84–210.6 nm for sample. The CdS flowers have an average cross-section diameter and length of 492.2 nm and 5.870 μm, respectively.
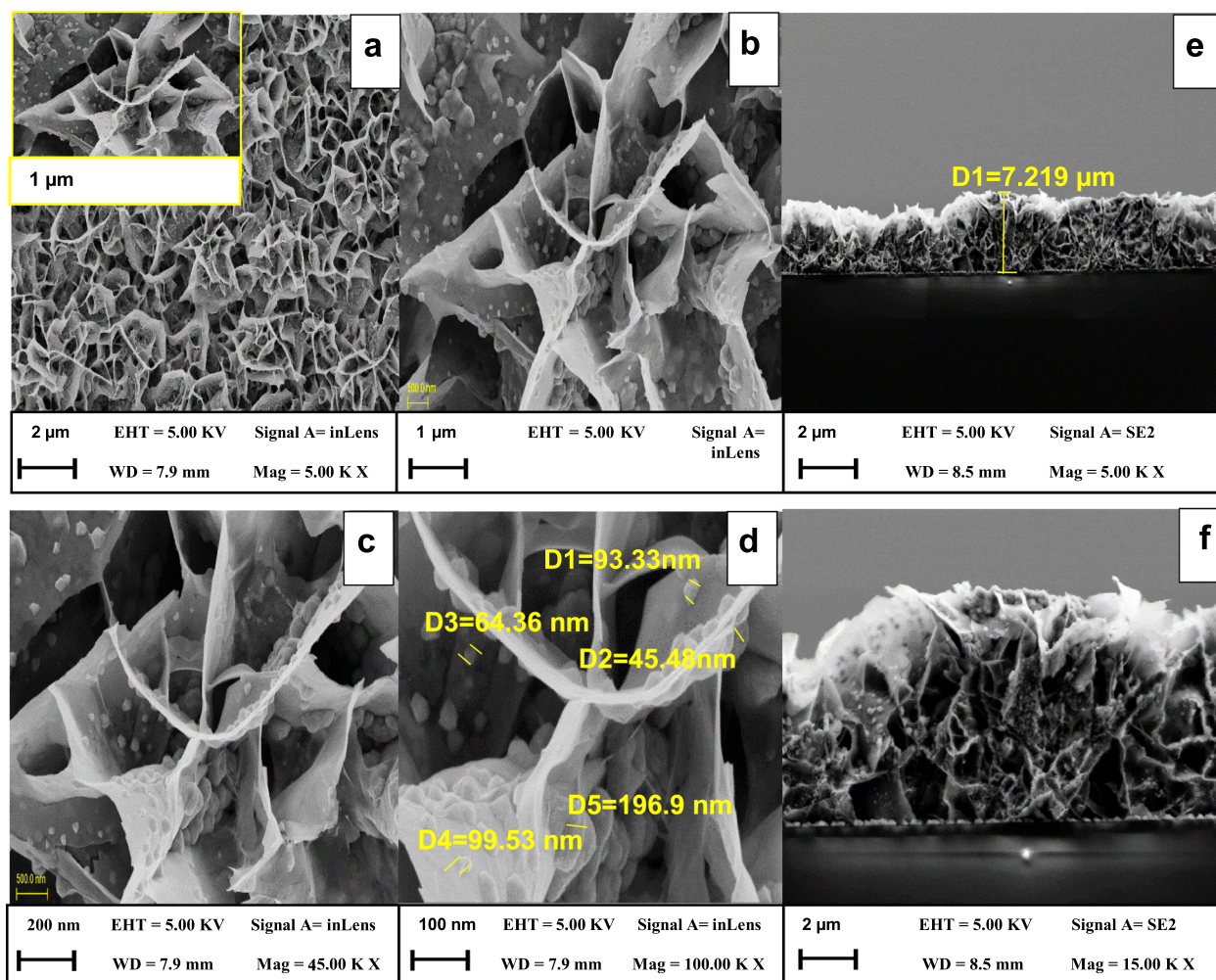
Fig. 5 CdS with 1% Mn-doped FESEM images (**a**, **b**) low magnification (**c**, **d**) high magnification top view (**e**, **f**) cross-sectional view

In Fig. 8 by focusing on one of the spherical shape particles (circled with yellow color), it can be seen that those spherical shapes are a build-up of nanoparticles which are aggregated, they had been formed like a flower, and the thickness of the nanosheets is about 59.15–227 nm (for CdS doped with 4%). The change in surface morphology with an increased doping concentration of Mn ions was attributed to the differences in the ionic radius of the Mn ion and Cd ion, the standard ion radius of Mn^{2+} (0.046 nm) is lower than that of Cd^{2+} (0.097 nm) [17].

The cadmium sulfide for undoped and 1% Mn-doped was coverage all the substrate area, because the two samples have nano flakes structure, where the extended flakes intersected to form a network structure without any blank. Whereas, the cadmium sulfide for samples doped with 2% and 3% do not cover all the substrate area, because the two samples have hierarchical flower-like nanostructure, where hierarchical flower was unopened, non-intersected, and with blank between flowers. While, the cadmium sulfide for sample doped with 4% cover all the substrate area, because

the sample has spherical shape particles which are aggregated without any blanks.

FE_SEM image of CdS thin films surfaces is shown in Figs. 4–8. Note that, unlike AFM, where the AFM can measure in all three dimensions (x, y, and z) with a single scan. Since the AFM has a vertical resolution of <0.5 Å, as well as calculate an RMS roughness of 0.7 Å. On a sample with this structure, the FE_SEM has difficulty resolving these features due to the subtle variations in height. For the FE_SEM, a large area view of the variations in surface structure can be acquired all at once, where as a 100 μm × 100 μm area is typically the largest area viewed by an AFM [29].

3.2.3 Energy dispersive X-ray spectroscopy (EDX)

EDX was used to perform a qualitative composition study. Figure 9a shows the EDX spectra of pure CdS before doping with Mn. All of the samples included CdS films, which are made up of cadmium (Cd) and sulfur (S). The
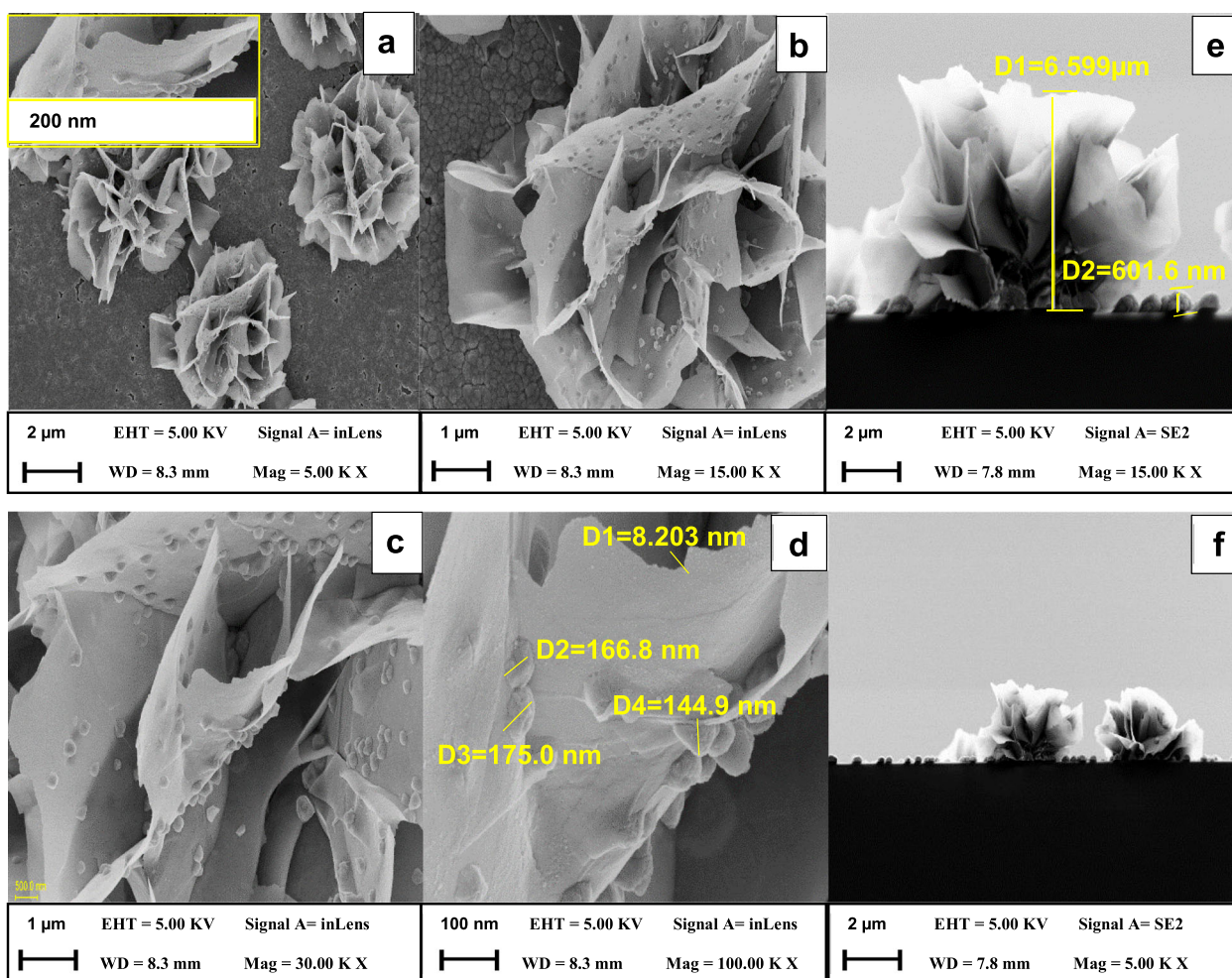
Fig. 6 CdS with 2% Mn-doped FESEM images (**a**, **b**) low magnification (**c**, **d**) high magnification top view (**e**, **f**) cross-sectional view

EDX spectra of all samples revealed very small concentrations of Si, O and N elements; such concentrations can be attributed to the substrate that supported the sample. The atoms, their weights and atomic percentages for the sample are depicted in the inset table of Fig. 9a. The EDX spectra of Mn-doped CdS, as seen in Fig. 9b–e, confirms the existence of Mn elements in Mn: CdS thin films, as predicted. This result suggests that the thin film contains Mn elements as, the inset table. In Fig. 9b–e, depicts all elements and their weight percentages for all Mn-CdS doped.

4 Optical properties

4.1 UV–VIS spectra

Figure 9 illustrates the transmittance of CdS and Mn-CdS films versus wavelength. Figure 10 shows transmittance as a function of wavelength in the range of 480–1100 nm for the undoped CdS thin films and Mn-doped CdS thin films produced by hydrothermal technique at 500 °C for 2 h. The optical transmittance values increase as the Mn doping concentration increases. This phenomenon may be due to an increase in set free electrons as the Mn concentration rises. The improvement in transmittance might be attributable to a reduction in optical scattering as a result of the densification of film crystallites.

The coefficient of absorption (α) was calculated by the formula [30, 31]:

$$\alpha = 2.303 \frac{A}{d} \tag{9}$$

where d and A, respectively represent the film thickness and absorption.

These films' bandgaps have been determined by the equation [32, 33];

$$\alpha h\nu = cons \tan t (h\nu - E_g)^{1/2} \tag{10}$$

where α represents the absorption coefficient, hυ represents photon energy, and E_g represents the energy gap. Figure 11 illustrates the plot of $(\alpha h\nu)^2$ versus $(h\nu)$ of CdS
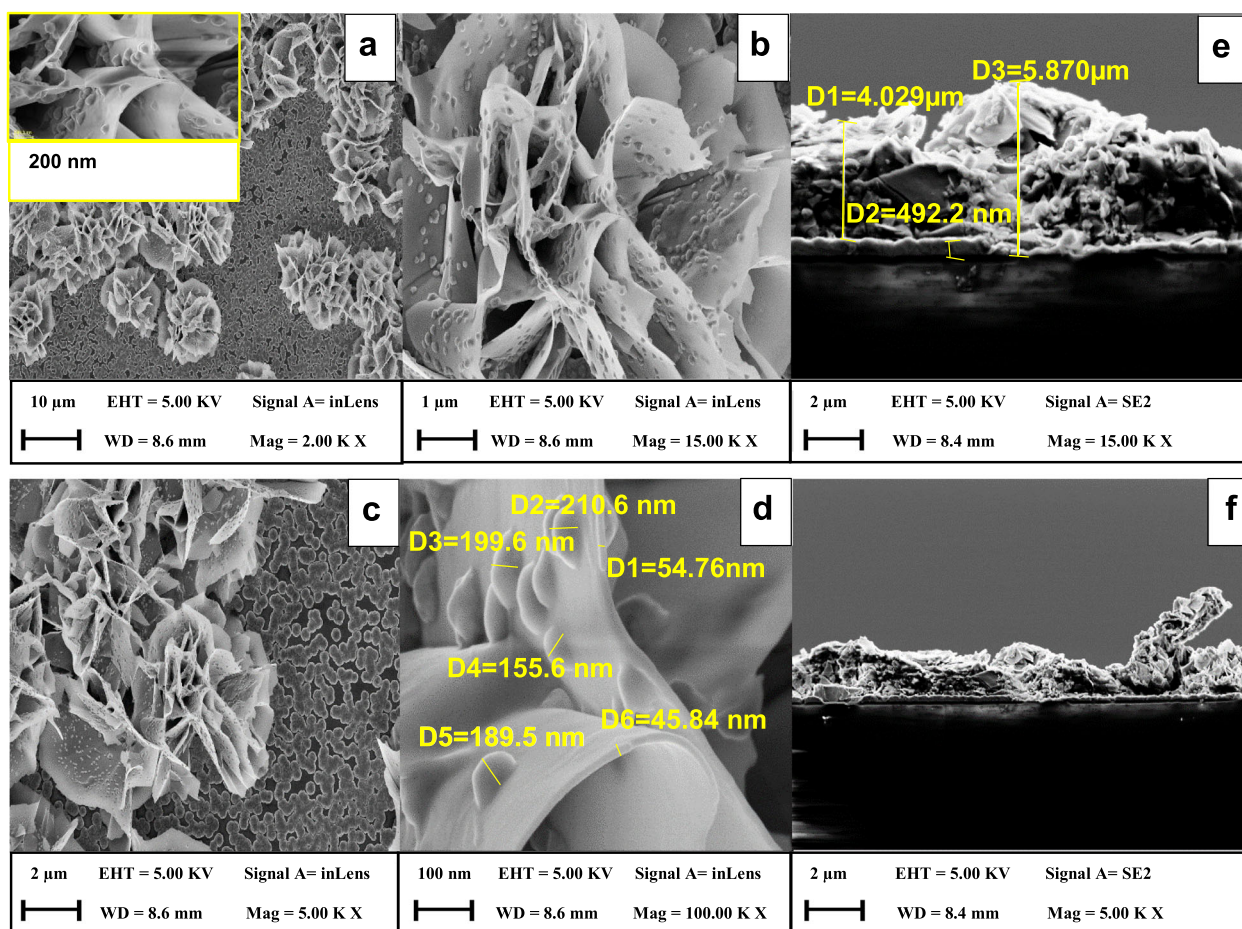
Fig. 7 CdS with 3% Mn-doped FESEM images (**a**, **b**) low magnification (**c**, **d**) high magnification top view (**e**, **f**) cross-sectional view

thin films and Mn-CdS. It was found that the band-gap values reduced from 2.4 to 1.76 eV along with increasing the doping concentration. A decrease in the energy band gap can be associated with several factors, viz. defect/ disorder induced band tailing, creation of impurity states, and grain size. The defect-induced band tailing due to the creation of localized energy states near the band edges. Earlier studies on ion-implanted CdS films have demonstrated similar occurrence of band-gap modification [34]. They observed a strong absorption below the band edge for the Mn-doped samples, which was attributed to the transitions involving band tails. Also Chandramohan et al. observed a strong absorption of CdS below the band edge for the Fe-implanted samples, which was attributed to the transitions involving band tails [35]. The width of these band tail states can be well described by the Urbach-tail parameter. In general, Urbach tails are considered to be a telltale signature of the presence of different types of impurities, structural disorder, point defects, and grain boundaries in a material. The estimated value of EU for the pure CdS film is about 200 meV, which is in good agreement with the value reported in

Ref. [34]. We observe a systematic increase in EU with increasing Mn concentration shown inset of Fig. 11, which could be due to static structural disorder, creating more and more localized states within the band tails of the electronic states.

4.2 Photoluminescence (PL) analysis

Photoluminescence is a process in which an electron excited by a monochromatic photon beam, is subjected to a certain energy radioactive recombination which is either in the valence band (edge of the scale luminescence) or traps surface states (usually the offset red luminescence) within the forbidden gap [36]. Figure 12 depicts the photoluminescence of pure and Mn-doped CdS thin film synthesized by the hydrothermal process. It is measured in an excitation wavelength of 331 nm at room temperature. The emission peak of 520 nm (2.3 eV) for the pure CdS shows spectroscopy shifting. This is the same as the transmittance spectrum optical band difference. This finding is consistent with the above data in UV–VIS, as shown in Fig. 9. This emission occurred due
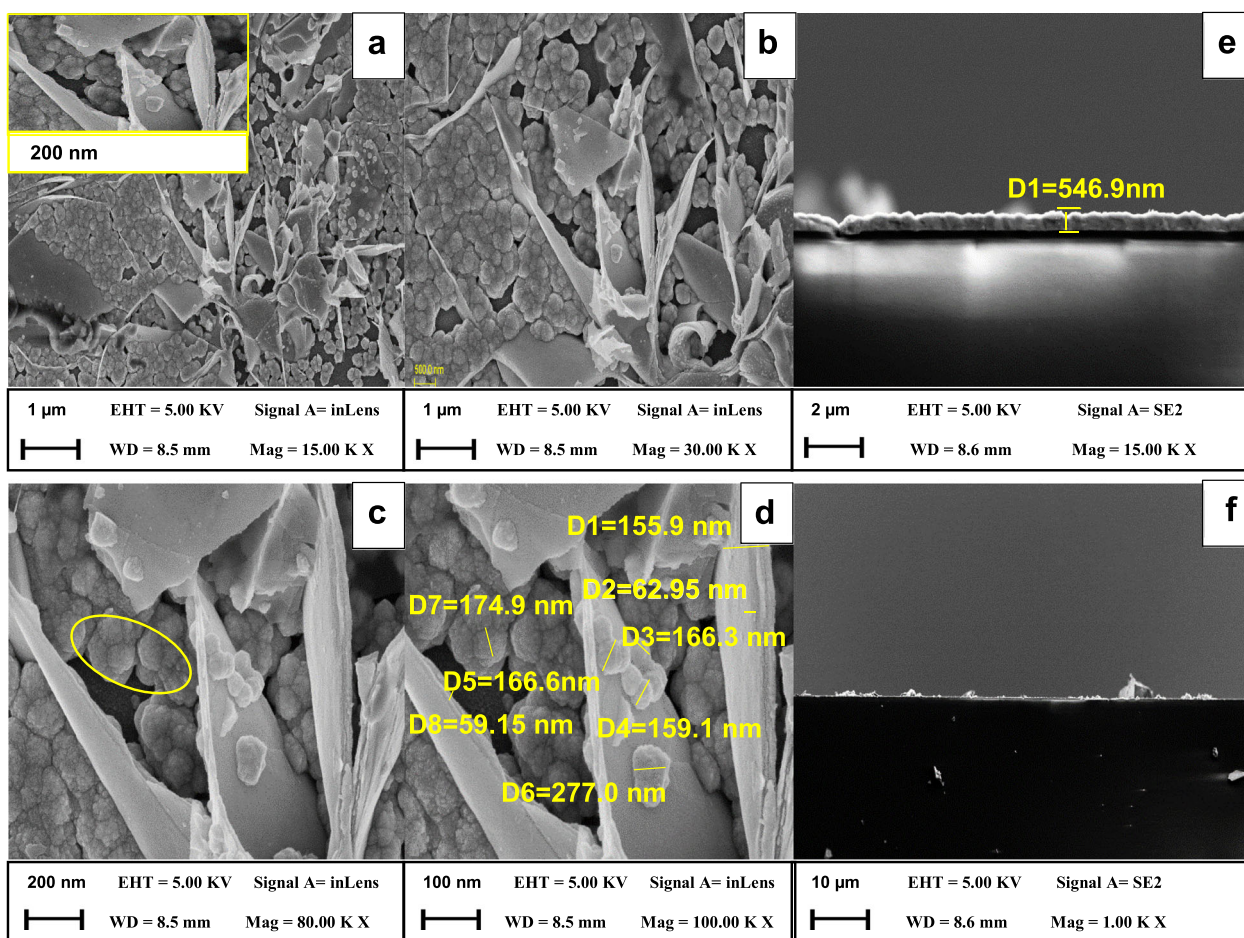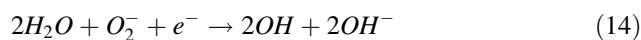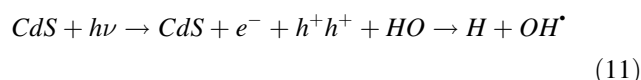
Fig. 8 CdS with 4% Mn-doped FESEM images (**a**, **b**) low magnification (**c**, **d**) high magnification top view (**e**, **f**) cross-sectional view

to the recombination of a free conduction electron with holes in the valence level and different reasons stated by [6]. While Mn-doped CdS concentrations (1%, 2%, 3%, and 4%) have emission ranges at 558 nm (2.23 eV), 565 nm (2.199), 567 nm (2.194 eV), and 567 nm (2.19), respectively, these are virtually similar to the transitional values for the energy gap values. The broadening of shape is due to the homogenous distribution of cadmium and sulfur atoms and the thermal energy associated with it.

5 Photocatalytic activity

Chalcogenide is considered the most effective photocatalyst option for visible light applications. The photoreactivity of semiconductors is strongly sensitive to their morphology, crystal structure, phase composition and shape [37]. The temporal dependence of optical absorbance of 0.01 M MB and MV solution was determined when kept in the dark and exposed to direct sunlight. The results conclusively demonstrate that whether exposed to direct sunlight or left in the dark, there was no significant difference in the absorbance of MB and MV solutions. The MB and MV degradation of as-synthesized photocatalysts was evaluated under the Xe lamp. The reaction begins, as electron-hole pairs appear on the CdS surface due to the absorption of light with an energy equals to or greater than the energy bandgap. The electrons formed on cadmium sulfide thin films react with methyl blue (MB) and methyl violet (MV). The suggested reaction mechanism is depicted below:
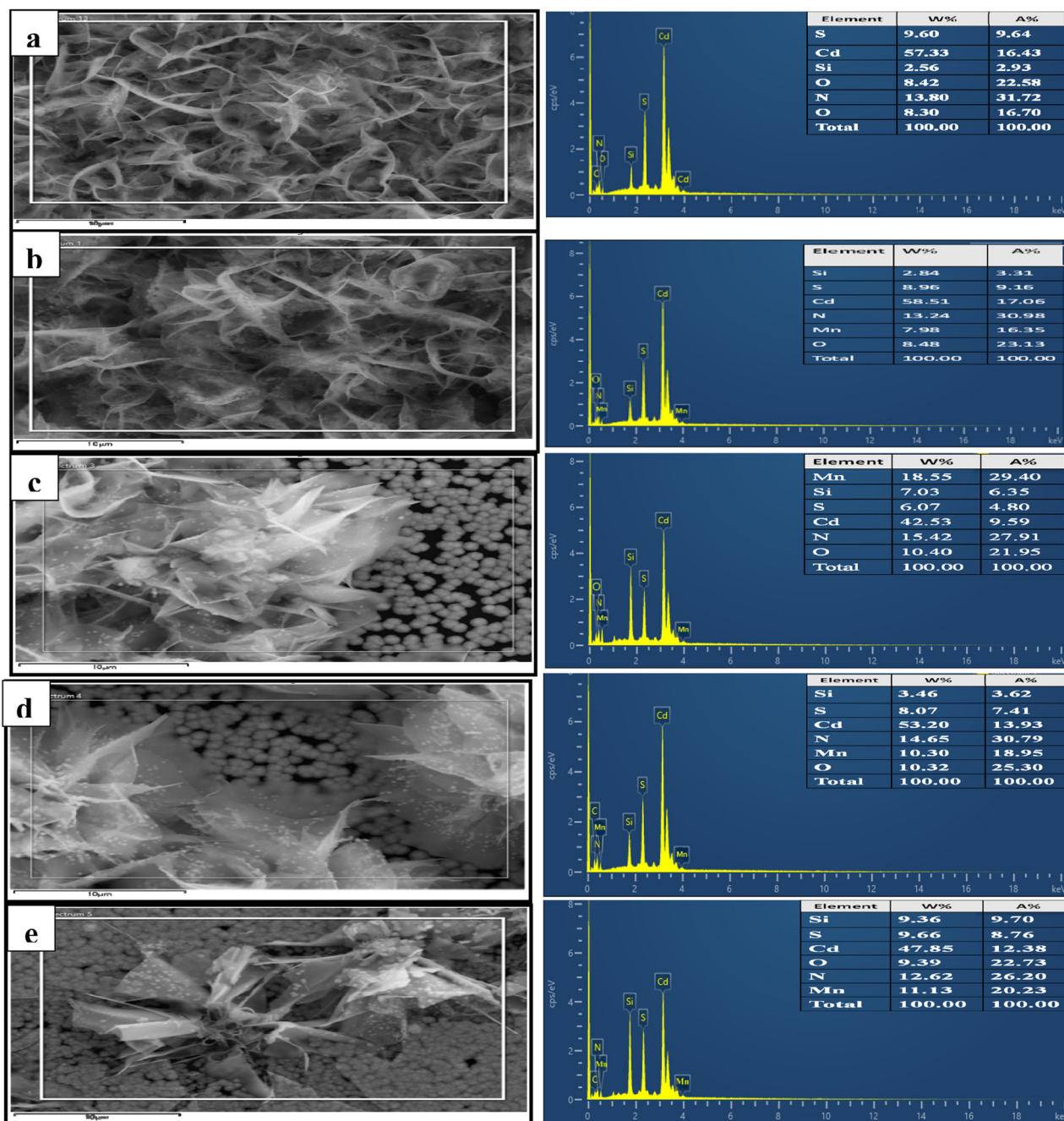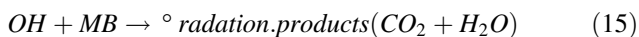
$$CdS + h\nu \rightarrow CdS + e^- + h^+ h^+ + HO \rightarrow H + OH^\bullet \tag{11}$$

$$h^+ + OH^- \rightarrow OH^\bullet \tag{12}$$

$$O_2 + e \rightarrow O_2^- \tag{13}$$

$$2H_2O + O_2^- + e^- \rightarrow 2OH + 2OH^- \tag{14}$$

Element	W%	A%
S	9.60	9.64
Cd	57.33	16.43
Si	2.56	2.93
O	8.42	22.58
N	13.80	31.72
O	8.30	16.70
Total	100.00	100.00

Element	W%	A%
Si	2.84	3.31
S	8.96	9.16
Cd	58.51	17.06
N	13.24	30.98
Mn	7.98	16.35
O	8.48	23.13
Total	100.00	100.00

Element	W%	A%
Mn	18.55	29.40
Si	7.03	6.35
S	6.07	4.80
Cd	42.53	9.59
N	15.42	27.91
O	10.40	21.95
Total	100.00	100.00

Element	W%	A%
Si	3.46	3.62
S	8.07	7.41
Cd	53.20	13.93
N	14.65	30.79
Mn	10.30	18.95
O	10.32	25.30
Total	100.00	100.00

Element	W%	A%
Si	9.36	9.70
S	9.66	8.76
Cd	47.85	12.38
O	9.39	22.73
N	12.62	26.20
Mn	11.13	20.23
Total	100.00	100.00

Fig. 9 EDX spectra of (**a**) pure, (**b**) 1%Mn-doped, (**c**) 2%Mn-doped CdS thin films, (**d**) 3% Mn-doped CdS and (**e**) 4% Mn-doped CdS

The OH$^•$ CdS radicals and holes are thought to be powerful oxidizing agents capable of degrading MB [38].

$$OH + MB \rightarrow {}^\circ radation.products(CO_2 + H_2O) \qquad (15)$$

$$h^+ + MB \rightarrow {}^\circ radation.products(CO_2 + H_2O) \qquad (16)$$

As, the energy gap of CdS films decreased with increasing Mn doping, this causes more photons to cross the energy gap, resulting in more (e−, h+) pairs being formed and more OH being generated. This leads us to the conclusion that MB decay accelerated [39]. For MV photocatalytic degradation, the reusability of pure CdS and Mn-doped CdS catalysts was investigated. In Fig. 13, one may observe that the UV–Vis absorbance spectra as a function of the photocatalytic reaction time were evaluated by MB and MV dye aqueous solutions and degraded by CdS thin film. It can be observed that, with increasing irradiation duration, the intensity of the absorption peak at 663 nm for MB and 558 nm for MV gradually reduced.
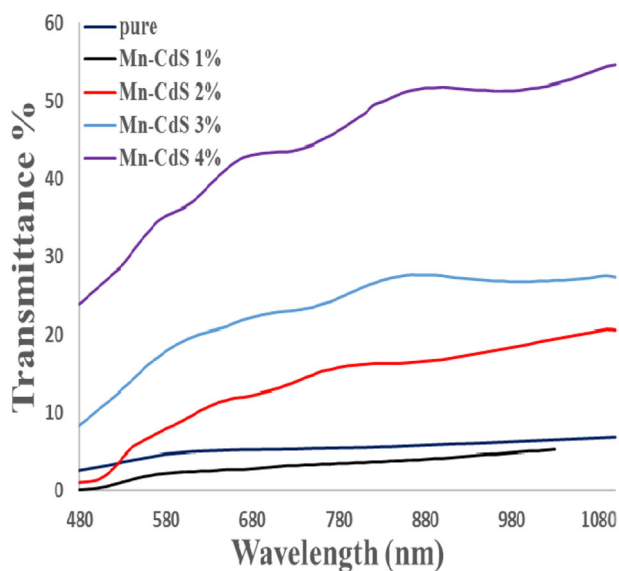
Fig. 10 Transmittance spectra of CdS prepared at various Mn concentrations (1–4%)
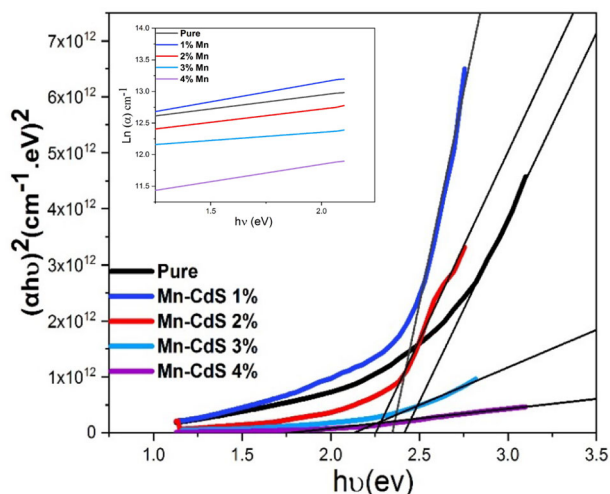

Fig. 11 $(\alpha h\nu)^2$ as a function of photon energy derived from the transmittance spectra. The inset shows the linear variation in absorption coefficient against photon energy h according to Urbach rule

There is an improvement in the photocatalytic degradation of the MB and MV dyes; this can be related to many reasons: a higher specific surface area, surface morphology, crystal structure, surface roughness, and the films' improved photoresponse [40]. Moreover, since there is a linear connection between the dye concentration and the irradiation period (Fig. 14), the degradation reaction follows pseudo-first-order kinetics. the measured Kapp values for MB and MV for the degrading process by CdS thin film are 0.00926, and 0.01404 for 260 min, respectively, this shows that the photodegradation rate of the methyl violet (MV) dye is higher than the one of MB.

Equation 1 was also used to compute the degrading efficiency %, which was displayed in Fig. 15. The MV dye shows to be efficiently degraded (i.e., 98% in 5 h) as compared to the other dye. Table 3 shows the degradation (percentage) of the k values for MB and MV.

Doping CdS with Mn notably affects the photocatalytic activity. Results reported in Fig. 15 revealed different trends depending on the doping concentration. The largest catalytic effect is observed in the presence of 4% Mn, for which the degradation of MV and MB attained 98 and 84, respectively. It is well known that different structures would have a different influence on the photocatalytic performance of CdS catalysts. The optical, photoelectrical and photochemical properties of the semiconductor can be influenced indirectly when the size, structure and morphology of the photocatalytic semiconductors are changed [41, 42]. In our research the pure and 1% Mn doping samples has 2-dimensional CdS nano flake have degradation values 63, 88 and 64, 91 for MB and MV, respectively. The photocatalytic activity of CdS nanocatalyst for photodegrading the MB and MV dye could be affected by the shape of the CdS nanostructure, and the results suggested that CdS nano flake had high photocatalytic efficiency. This result was mainly due to the fact that the CdS nanos flake had a lower recombination rate of electron-hole pairs and larger surface area, contributing to the adsorption of more methylene blue and methylene violet dye molecules, and thus better photocatalytic performance during the photocatalytic process [43]. While for other samples with higher doping CdS photocatalysts has 3-dimensional structure porous CdS nanosheet-assembled flowers. We observe has higher photodegrading than other two samples, due to the special structural features, such as a high surface/volume ratio and low density [44].

6 Reusability of the photocatalyst

In consideration of practical applications, the photocatalyst should be chemically and optically stable after several repeated cycles. To investigate the reuse of 0%, 1%, 2%, 3% and 4% Mn-doped CdS in the photocatalytic degradation of MV and MB, the experiment was repeated three times. The degradation of the MV and MB dye was measured after 260 min of exposure to xenon lamp irradiation. After each decomposition reaction, the thin films were washed with water, dried and used again under the same conditions. As shown in Fig. 16, the better results were observed, where a slight decrease in photodegradation efficiency was observed. This may be explained by the formation of some intermediate species that remained adsorbed at the surface of catalyst thin films [45].
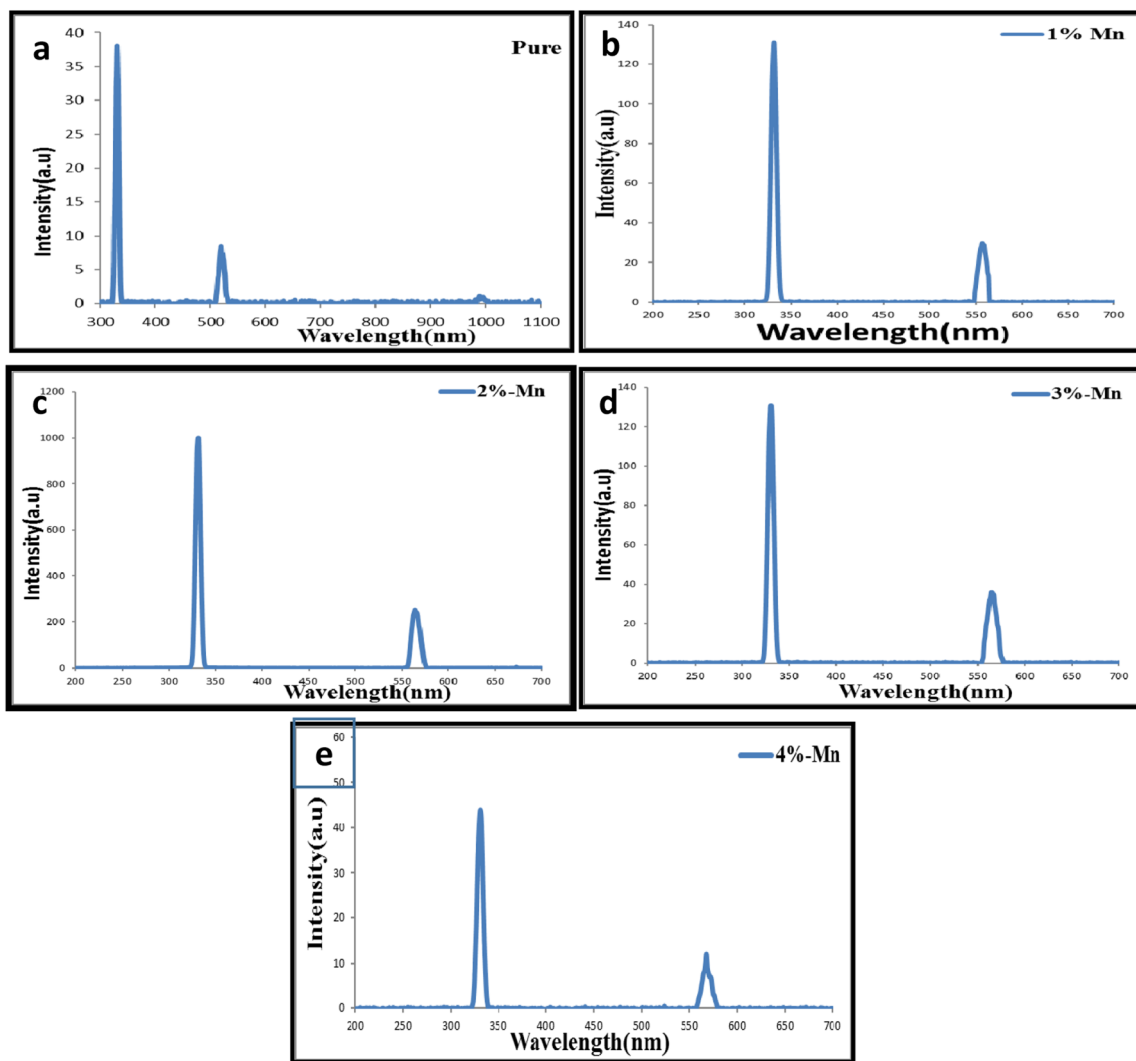
Fig. 12 **Photoluminescence spectra of pure CdS and doped CdS of Mn. a** For pure sample. **b** 1% Mn. **c** 2% Mn. **d** 3% Mn. **e** 4% Mn sample.
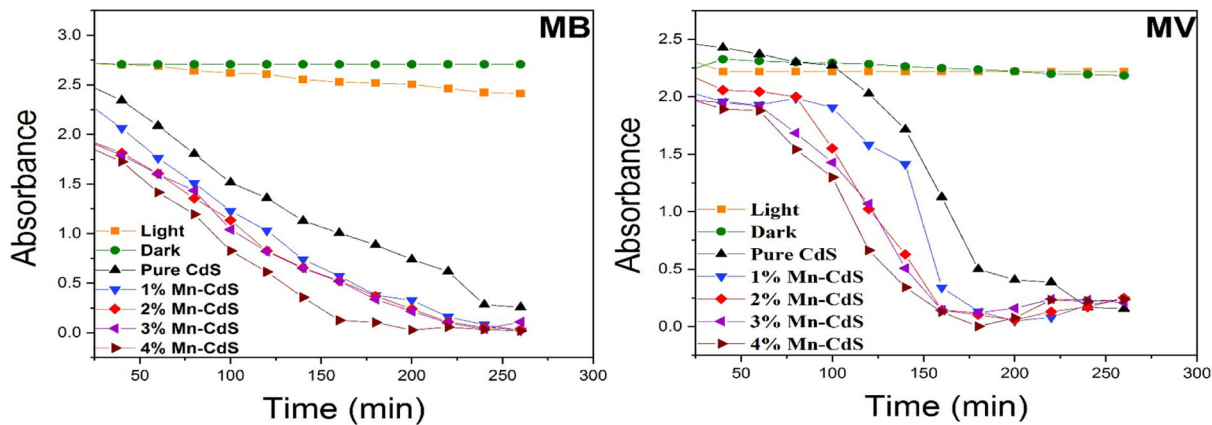

Fig. 13 Absorbance of an aqueous solution with an irradiation time of the CdS films immersed in methyl blue (MB) and methyl violet (MV)
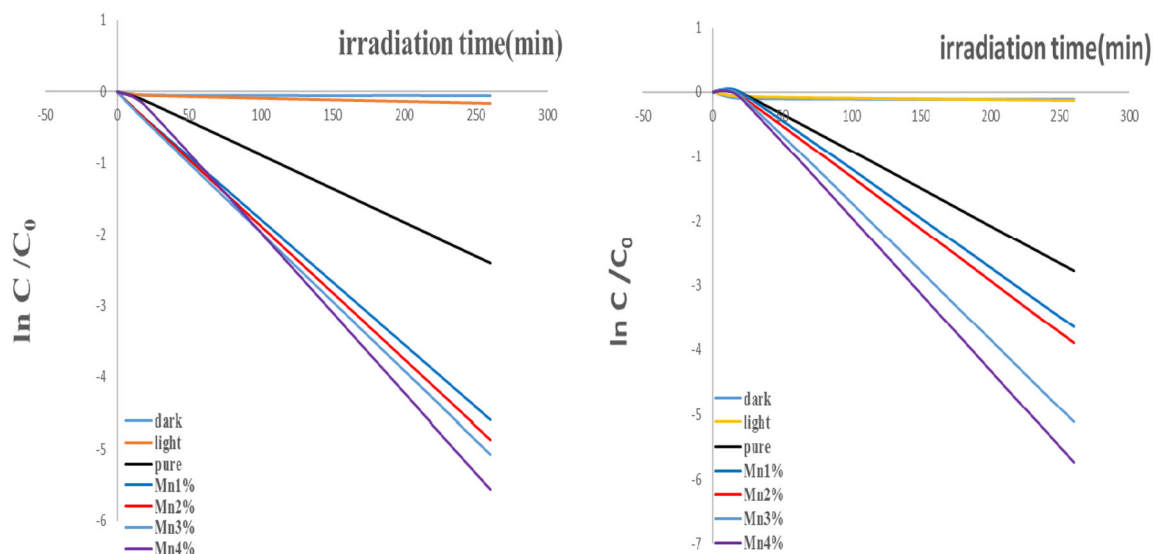
Fig. 14 The relation between ln C/C_0 with irradiation time for cadmium sulfide thin films MB and MV solution
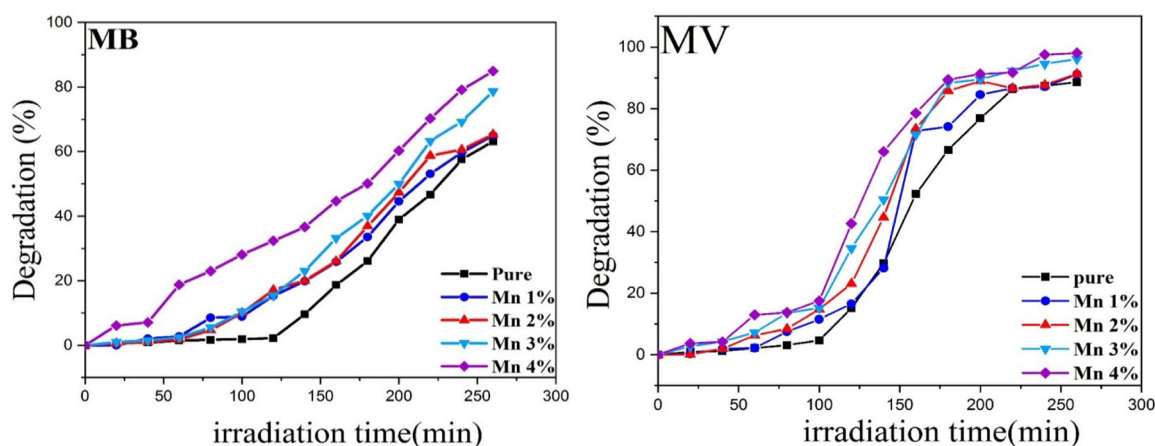

Fig. 15 Degradation of aqueous MB and MV solution as a function of irradiation light time of the CdS thin films immersed in it

Table 3 Degradation and rate constant (k) (%) of the methyl orange (MB), and methyl violet (MV) (100 mg/l) solution

Samples	K min^{-1} for MB	Degradation in 260 min	K min^{-1} for MV	Degradation in 260 min
Pure CdS	0.01949	63	0.0221	88
Mn 1%	0.01872	64	0.01968	91
Mn 2%	0.01766	65	0.01497	91.5
Mn 3%	0.01256	78	0.00994	94
Mn 4%	0.00926	84	0.01404	98

7 Conclusion

Pure and Mn-doped CdS thin films were deposited on clean glass substrates for 2 h at 150 °C using hydrothermal technique. The morphology was revealed by FESEM (density, thickness and diameter) of the nanoflowers, which was adjusted by varying the doping construction. In addition, XRD analyses of as-deposited samples show polycrystalline hexagonal and cubic structures with a distinct degree H (002) or C peak (111). The investigated photocatalyst activity of all films was exposed to a xenon lamp for 260 min. Mn ion plays a major role in influencing the efficiency of photocatalysts. The optimum concentration of Mn ion is 4%; the efficiency of the photocatalyst at this concentration reaches 84% of MB and 98% of MV when irradiated with a xenon lamp for 260 min.
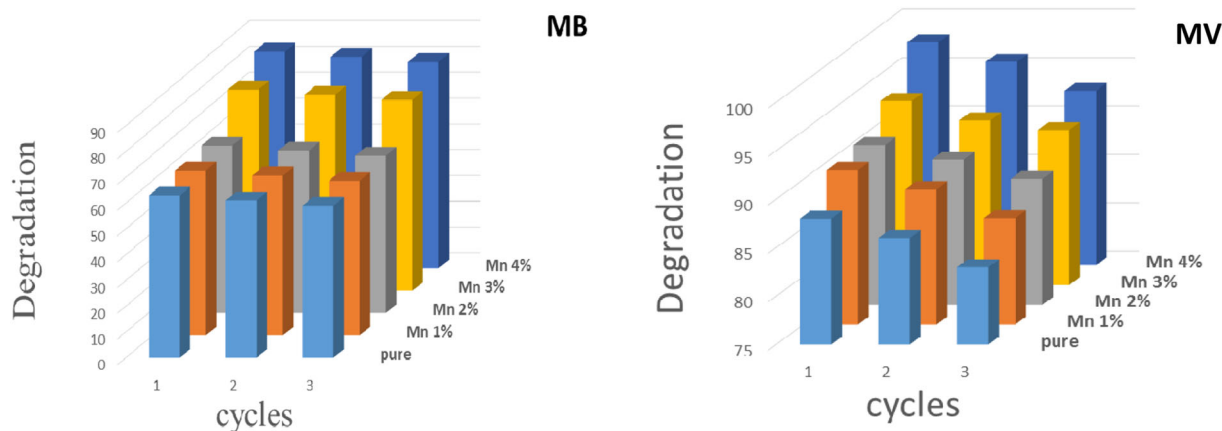
Fig. 16 Evolution of the residual concentration of toluidine after three degradation cycles in the presence of pure CdS and Mn-doped CdS photocatalyst

Compliance with ethical standards

Conflict of interest The authors declare no competing interests.

Publisher's note Springer Nature remains neutral with regard to jurisdictional claims in published maps and institutional affiliations.

References

1. Al Balushi BSM, Al Marzouqi F, Al Wahaibi B et al. (2018) Hydrothermal synthesis of CdS sub-microspheres for photocatalytic degradation of pharmaceuticals. Appl Surf Sci 457:559–565. https://doi.org/10.1016/j.apsusc.2018.06.286

2. Iacomi F, Purica M, Budianu E et al. (2007) Structural studies on some doped CdS thin films deposited by thermal evaporation. Thin Solid Films 515:6080–6084. https://doi.org/10.1016/j.tsf.2006.12.091

3. Karthik K, Pushpa S, Madhukara Naik M, Vinuth M (2020) Influence of Sn and Mn on structural, optical and magnetic properties of spray pyrolysed CdS thin films. Mater Res Innov 24:82–86. https://doi.org/10.1080/14328917.2019.1597436

4. Yang X, Wang B, Mu Y, et al. (2019) Photocatalytic performance of cubic and hexagonal phase CdS synthesized via different Cd sources. J Electron Mater. https://doi.org/10.1007/s11664-019-06967-4

5. Diaz-Grijalva OI, Berman-Mendoza D, Flores-Pacheco A et al. (2020) Cu-doped CdS thin films by chemical bath deposition and ion exchange. J Mater Sci Mater Electron 31:1722–1730. https://doi.org/10.1007/s10854-019-02690-2

6. Khan M, Shahid Khan M, Aziz A et al. (2013) Spectroscopic studies of sol-gel grown CdS nanocrystalline thin films for optoelectronic devices. Mater Sci Semicond Process 16:1894–1898. https://doi.org/10.1016/j.mssp.2013.07.010

7. Trajić J, Gilić M, Romčević N et al. (2015) Raman spectroscopy of optical properties in cds thin films. Sci Sinter 47:145–152. https://doi.org/10.2298/SOS1502145T

8. Zyoud A, Saa'Deddin I, Khudruj S et al. (2013) CdS/FTO thin film electrodes deposited by chemical bath deposition and by electrochemical deposition: a comparative assessment of photoelectrochemical characteristics. Solid State Sci 18:83–90. https://doi.org/10.1016/j.solidstatesciences.2013.01.004

9. Islam MA, Haque F, Rahman KS et al. (2015) Effect of oxidation on structural, optical and electrical properties of CdS thin films grown by sputtering. Optik 126:3177–3180. https://doi.org/10.1016/j.ijleo.2015.07.078

10. Xie R, Su J, Li M, Guo L (2013) Structural and photoelectrochemical properties of Cu-doped CdS thin films prepared by ultrasonic spray pyrolysis. Int J Photoenergy. https://doi.org/10.1155/2013/620134

11. Loudhaief N, Labiadh H, Hannachi E et al. (2018) Synthesis of CdS nanoparticles by hydrothermal method and their effects on the electrical properties of bi-based superconductors. J Supercond Nov Magn 31:2305–2312. https://doi.org/10.1007/s10948-017-4496-4

12. Husham M, Hassan Z, Mahdi MA et al. (2014) Fabrication and characterization of nanocrystalline CdS thin film-based optical sensor grown via microwave-assisted chemical bath deposition. Superlattices Microstruct 67:8–16. https://doi.org/10.1016/j.spmi.2013.12.010

13. Liang YC, Lung TW (2016) Growth of hydrothermally derived CdS-based nanostructures with various crystal features and photoactivated properties. Nanoscale Res Lett 11. https://doi.org/10.1186/s11671-016-1490-x

14. Mullamuri B, Sai Sriram Mosali V, Maseed H et al. (2021) Photocatalytic activity of heavy metal doped Cds nanoparticles synthesized by using ocimum sanctum leaf extract. Biointerface Res Appl Chem 11:12547–12559. https://doi.org/10.33263/BRIAC115.1254712559

15. Murugesan R, Sivakumar S, Karthik K et al. (2019) Effect of Mg/Co on the properties of CdS thin films deposited by spray pyrolysis technique. Curr Appl Phys 19:1136–1144. https://doi.org/10.1016/j.cap.2019.07.008

16. Rmili A, Ouachtari F, Bouaoud A et al. (2013) Structural, optical and electrical properties of Ni-doped CdS thin films prepared by spray pyrolysis. J Alloy Compd 557:53–59. https://doi.org/10.1016/j.jallcom.2012.12.136

17. Suo Z, Dai J, Gao S, Gao H (2020) Effect of transition metals (Sc, Ti, V, Cr and Mn) doping on electronic structure and optical properties of CdS. Results Phys 17:103058. https://doi.org/10.1016/j.rinp.2020.103058

18. Phasook N, Kamoldirok S, Yindeesuk W (2018) Optical properties of Mn-doped CdS thin films grown by the SILAR method. J Phys Conf Ser 1144. https://doi.org/10.1088/1742-6596/1144/1/012009

19. Muckel F, Delikanli S, Hernández-Martínez PL et al. (2018) Sp-d exchange interactions in wave function engineered colloidal CdSe/Mn:CdS hetero-nanoplatelets. Nano Lett 18:2047–2053. https://doi.org/10.1021/acs.nanolett.8b00060

20. Bhattacharyya S, Estrin Y, Rich DH et al. (2010) Luminescent and ferromagnetic CdS:Mn2+/C core-shell nanocrystals. J Phys Chem C 114:22002–22011. https://doi.org/10.1021/jp107083f

21. Saikia L, Bhuyan D, Saikia M et al. (2015) Photocatalytic performance of ZnO nanomaterials for self sensitized degradation of malachite green dye under solar light. Appl Catal A Gen 490:42–49. https://doi.org/10.1016/j.apcata.2014.10.053

22. Al-Jawad SMH, Ismail MM, Ghazi SF (2021) Characteristics of Ni-doped TiO2 nanorod array films. J Aust Ceram Soc 57:295–304. https://doi.org/10.1007/s41779-020-00530-9

23. AL-Jawad SMH, Taha AA, Redha AM (2019) Studying the structural, morphological, and optical properties of CuS:Ni nanostructure prepared by a hydrothermal method for biological activity. J Sol-Gel Sci Technol 91:310–323. https://doi.org/10.1007/s10971-019-05023-1

24. Aksu S, Bacaksiz E, Parlak M et al. (2011) Structural, optical and magnetic properties of Mn diffusion-doped CdS thin films prepared by vacuum evaporation. Mater Chem Phys 130:340–345. https://doi.org/10.1016/j.matchemphys.2011.06.046

25. Williamson GK, Hall WH (1953) X-Ray broadening from filed aluminium and tungsten. Acta Met 1:22–31

26. Irfan H, Mohamed Racik K, Anand S (2018) Microstructural evaluation of CoAl2O4 nanoparticles by Williamson–Hall and size–strain plot methods. J Asian Ceram Soc 6:54–62. https://doi.org/10.1080/21870764.2018.1439606

27. Judran HK, Yousif NA, AL-Jawad SMH (2021) Preparation and characterization of CdS prepared by hydrothermal method. J Sol-Gel Sci Technol 97:48–62. https://doi.org/10.1007/s10971-020-05430-9

28. Shende DA, Rane YN, Raghuwanshi MG et al. (2018) Visible-light-driven photocatalytic activity of mixed phase CdS-flakes. Optik 161:284–292. https://doi.org/10.1016/j.ijleo.2018.02.052

29. Russell P, Batchelor D, Facility AI, Russell PE (2001) SEM and AFM: complementary techniques for surface investigations. Microsc Anal 7:9–12

30. Al-Jawad SMH, Salman ON, Yousif NA (2018) Influence of titanium tetrachloride concentration and multiple growth cycles of TiO2 nanorod on photoanode performance in dye sensitized solar cell. Photonics Nanostruct Fundam Appl 31:81–88. https://doi.org/10.1016/j.photonics.2018.06.010

31. Al-Jawad SMH, Salman ON, Yousif NA (2019) Influence of growth time on structural, optical and electrical properties of TiO2 nanorod arrays deposited by hydrothermal method. Surf Rev Lett 26:1–9. https://doi.org/10.1142/S0218625X1850155X

32. Al-Jawad SMH, Imran NJ, Mohammad MR (2020) Effect of electrolyte solution and deposition methods on TiO2/CdS core-shell nanotube arrays for photoelectrocatalytic application. EPJ Appl Phys 92. https://doi.org/10.1051/epjap/2020200127

33. Al-Jawad SMH, MOHAMMAD MR, JAMAL IMRANN (2018) Effect of electrolyte solution on structural and optical properties of TiO2 grown by anodization techniqye for photoelectrocatalytic application. Surf Rev Lett 25(5):16. https://doi.org/10.1142/S0218625X18500786

34. Chandramohan S, Kanjilal A, Tripathi JK, et al. (2009) Structural and optical properties of Mn-doped CdS thin films prepared by ion implantation. J Appl Phys 105. https://doi.org/10.1063/1.3151712

35. Chandramohan S, Kanjilal A, Sarangi SN et al. (2010) Effect of Fe-ion implantation doping on structural and optical properties of CdS thin films. Appl Phys A Mater Sci Process 99:837–842. https://doi.org/10.1007/s00339-010-5598-z

36. Bhattacharyya D, Chaudhuri S, Pal AK (1995) Electrical conduction at low temperatures in polycrystalline CdTe and ZnTe films. Mater Chem Phys 40:44–49. https://doi.org/10.1016/0254-0584(94)01453-N

37. Talebian N, Nilforoushan MR, Ramazan Ghasem R (2012) Enhanced photocatalytic activities of ZnO thin films: a comparative study of hybrid semiconductor nanomaterials. J Sol-Gel Sci Technol 64:36–46. https://doi.org/10.1007/s10971-012-2825-4

38. Shaban M, Mustafa M, El Sayed AM (2016) Structural, optical, and photocatalytic properties of the spray deposited nanoporous CdS thin films; influence of copper doping, annealing, and deposition parameters. Mater Sci Semicond Process 56:329–343. https://doi.org/10.1016/j.mssp.2016.09.006

39. Shaban YA (2013) Enhanced photocatalytic removal of methylene blue from seawater under natural sunlight using carbon-modified n-TiO2 nanoparticles. Environ Pollut 3. https://doi.org/10.5539/ep.v3n1p41

40. Zheng G, Shang W, Xu L et al. (2015) Enhanced photocatalytic activity of ZnO thin films deriving from a porous structure. Mater Lett 150:1–4. https://doi.org/10.1016/j.matlet.2015.03.001

41. Serhan M, Sprowls M, Jackemeyer D, et al. (2019) Total iron measurement in human serum with a smartphone. AIChE Annu Meet Conf Proc. https://doi.org/10.1039/x0xx00000x

42. Chen CQ, Shi Y, Zhang YS et al. (2006) Size dependence of Young's modulus in ZnO nanowires. Phys Rev Lett 96:1–4. https://doi.org/10.1103/PhysRevLett.96.075505

43. Lang D, Xiang Q, Qiu G et al. (2014) Effects of crystalline phase and morphology on the visible light photocatalytic H2-production activity of CdS nanocrystals. Dalt Trans 43:7245–7253. https://doi.org/10.1039/c3dt53601g

44. Jin J, Yu J, Liu G, Wong PK (2013) Single crystal CdS nanowires with high visible-light photocatalytic H 2-production performance. J Mater Chem A 1:10927–10934. https://doi.org/10.1039/c3ta12301d

45. Hamden Z, Conceição D, Boufi S et al. (2017) Structural, morphological, optical and photocatalytic properties of Y, N-doped and codoped TiO2 thin films. Materials 10:1–13. https://doi.org/10.3390/ma10060600